



Evolution of N₂O production at lean combustion condition in NH₃/H₂/air premixed swirling flames

S. Mashruk^{a,*}, E.C. Okafor^b, M. Kovaleva^a, A. Alnasif^{a,c}, D. Pugh^a, A. Hayakawa^d, A. Valera-Medina^a

^a College of Physical Sciences and Engineering, Cardiff University, Wales, United Kingdom

^b Department of Mechanical Engineering, Kyushu University, 744 Motoooka, Nishi-ku, Fukuoka 819-0395, Japan

^c Engineering Technical College of Al-Najaf, Al-Furat Al-Awsat Technical University, Najaf, 31001, Iraq

^d Institute of Fluid Science, Tohoku University, Sendai, Japan



ARTICLE INFO

Article history:

Received 14 November 2021

Revised 11 July 2022

Accepted 11 July 2022

Keywords:

N₂O

Ammonia

Hydrogen

Combustion

Power generation

Radicals

Chemiluminescence

ABSTRACT

In the development of ammonia - hydrogen blends as potential substitutes for fossil fuels, the retrofitting of existing devices running at very lean condition is one of the promising solutions for decarbonisation of the power sector. However, little is known about the impact of these conditions on the production of NO_x, particularly N₂O that is a potent greenhouse gas. Therefore, the influence of varying thermal power and Reynolds numbers on the flame and emission characteristics, especially N₂O, of ammonia-hydrogen-air swirling flames has been evaluated for the first time through the use of spatially resolved OH*, NH* and NH₂* chemiluminescence, spectrometry analyses and advanced emissions characterisation at a fixed lean equivalence ratio, $\Phi = 0.65$, representative of the Dry Low NO_x (DLN) approach in traditional stationary gas turbines. NO and NO₂ emissions were found to be decreasing (from ~ 5000 ppmv to ~ 1000 ppmv; NO and from ~ 150 ppmv to ~ 50 ppmv; NO₂) with increasing ammonia content (from 50% to 90%) in the fuel while N₂O followed reverse trends (from ~ 50 ppmv to ~ 200 ppmv). More than 80% ammonia content in the fuel blends exhibited high amounts of unreacted ammonia fractions (~ 100 to ~ 1200 ppmv), which can be potentially linked to flame instability and/or low temperatures. Furthermore, any increasing or decreasing trends in NO_x with ammonia fraction were made more extreme by increasing thermal power or Reynolds number due to the differences in relevant radicals (NH, OH, NH₂ etc.) formation in the flames. Experimental results suggest the unviability of these blends at the conventional lean conditions utilised at the DLN power applications due to excessive NO_x emissions. Detailed sensitivity analyses of N₂O concentration at the flame and post flame zone has been carried out utilising Ansys Chemkin-PRO to identify and investigate the reactions responsible for N₂O formation/consumption in the experimental flames. Results have identified the reaction $\text{NH} + \text{NO} \leftrightarrow \text{N}_2\text{O} + \text{H}$ as the major source of N₂O production in the flame, while the reactions $\text{N}_2\text{O} + \text{H} \leftrightarrow \text{N}_2 + \text{OH}$ and $\text{N}_2\text{O}(\text{+M}) \leftrightarrow \text{N}_2 + \text{O}(\text{+M})$ are responsible for N₂O consumption at the post flame zone, with higher reactivity for the latter reaction at longer residence time and relatively lower temperatures.

© 2022 The Author(s). Published by Elsevier Inc. on behalf of The Combustion Institute.

This is an open access article under the CC BY license (<http://creativecommons.org/licenses/by/4.0/>)

1. Introduction

Ammonia has recently received considerable attention as an option for the replacement of fossil fuels. This chemical possesses an interesting set of characteristics; i.e. low flammability, existing distribution network etc., that makes it easy to handle at relatively high temperature or low pressure [1]. Furthermore, ammonia's volumetric hydrogen content is greater than liquid hydrogen [2], an

extensive infrastructure exists for its deployment, and the use of ammonia as a synthesised chemical dates back to the 1830's [3]. These reasons and the high versatility of such a chemical have promoted its use to power combustion systems and fuel cell devices [4], potentially delivering greater hydrogen quantities than other options (i.e. Liquid Organic Hydrogen Carriers, LOHC, etc.). However, there are still technical challenges with the use of ammonia. In combination with the toxic nature of ammonia, problems related to the excessive production of nitrogen oxides (NO_x) are the major barriers to the use of ammonia for power generation. Furthermore, flame stability, ammonia's lower energy density (i.e.

* Corresponding author.

E-mail address: Mashruks@cardiff.ac.uk (S. Mashruk).

18 MJ/kg compared to 55 MJ/kg of methane, [5]), and corrosion pose further challenges to the use of ammonia for these applications.

Extensive literature has been produced about ammonia application and its better safety characteristics when compared to other zero carbon alternatives [6,7,8], whilst most corrosion problems can be tackled by removing materials with high reactivity to ammonia or by using advanced coatings [9,10]. Similarly, flame stability has recently been addressed via vast research that has led to the recommendation of using doping agents, such as hydrogen and/or methane, to improve flame speed [11–14].

However, one of the greatest challenges lays on the detailed understanding of NO_x emissions produced during the combustion of ammonia blends. In a recent study, Ariemma et al. [15] showed that inclusion of methane in ammonia flames extends the stable operating range under MILD combustion conditions but produce higher NO_x emissions compared to pure ammonia or methane flames. Zhang et al. [16] showed that 10% methane or hydrogen addition in the ammonia flames had similar NO_x emissions performance as pure ammonia flames. They have concluded hydrogen to be better doping agent than methane as with 30% methane addition to ammonia flames, large NO_x and CO emissions were detected at exhaust. Another recent study of low power ammonia flames in an industrial, staged, swirl combustor [17] have reported NO emissions to be dependant on a broad range of factors such as equivalence ratio, humidification, staging and injection configuration. Numerical modelling exploring ammonia/hydrogen combustion kinetics [18] have shown improved combustion stability due to the increase in flame speed and reduction in ignition delay time, resulting from hydrogen addition. Further, advanced numerical studies [19] have been attempted to evaluate the spatial pattern of NO formation via DNS analyses in ammonia/hydrogen premixed flames. The study found that nitric oxide's formation is closely linked to flame curvature and affected by thermo-diffusive effects acting on key chemical species, which generate local equivalence ratios that prominently affect NO production. Similar works on NO production can be found elsewhere [20]. However, studies of such blends are often focused on NO and NH_3 as key emission components, and neglect to include or detail nitrous oxide, N_2O , despite its significant 20-year global warming of potential (GWP₂₀) being 280 times that of CO_2 [21]. Recent studies reporting NO emissions of ammonia/hydrogen blends [22] emphasised that ammonia flame producing flue gases with around 240 ppm of N_2O , would have approximately equivalent global warming impact, compared to the CO_2 emitted from a pure methane flame with an equivalence ratio, $\Phi = 0.60$.

Lean premixed combustion technology in combination with flame stabilisation through swirl is a method of reducing NO_x emissions in traditional fossil fuel-based gas turbines [23]. Despite being an established alternative to other NO_x reduction technologies, such as rich-quench-lean (RQL) combustion and humidified injection, there is limited literature on the suitability of this technique for gas turbines fuelled by ammonia-based blends. Further, the proper understanding of lean ammonia combustion could precede potentially faster retrofitting of currently standing power units that operate under Dry Low NO_x (DLN) principles. Hence, the present work reports the characteristics of ammonia/hydrogen flames at $\Phi = 0.65$, a sufficiently lean equivalence ratio to approach low- NO production trends without compromising flame stability. At the same time, studies of other ammonia-based blends have reported N_2O production in the very lean region. For example, ammonia-methane [24] swirl flames have been shown to produce N_2O values as high as 120 ppm at an equivalence ratio $\phi = 0.6$, while being negligible for other rich and near-stoichiometric conditions. In pure ammonia flames, N_2O production was shown to be sensitive to wall conditions [25], and also prominent at very

lean conditions. Moreover, a recent experimental study [26] has showed reduced NO formations at very lean conditions for various NH_3/H_2 blends. However, to authors' best knowledge, no detailed investigation on the production of N_2O at has been conducted for NH_3/H_2 blends at very lean condition. Thus, this study investigates the suitability of hydrogen doped ammonia flames that could be employed in Dry Low NO_x (DLN) scenario, with an assessment under atmospheric conditions to determine stability and exhaust emissions performances.

There are a great variety of models [2731] that are under evaluation for their use in computational modelling techniques to design systems capable of reducing emissions whilst maintaining high reliability and combustion operability. Despite the wide variety of mechanisms available for ammonia/hydrogen blends, many show discrepancies, and mechanisms tend to be useful within very specific set of operating conditions, or restricted by their original validation criteria. Therefore, detailed experimental validation for novel models that can properly resolve N_2O is required, particularly for systems employing industrially-relevant configurations, such as strong swirling flows.

To summarise, this manuscript provides further understanding of ammonia/hydrogen blends through a combined experimental and numerical modelling approach. Lean operating conditions, highly relevant to most currently available gas turbines, are explored and the effects of Reynolds number and thermal power on emissions production, temperature, spectral profiles, operability, and transient profiles reported. Numerical results, based on a chemical reactor network and in combination with recent detailed reaction mechanisms, are compared against experimental results. These explain the underlying chemistry contributing to the production of N_2O at these conditions, the results of which can be used to aid the design of future design combustors, novel injection strategies and operating regimes for the use of ammonia/hydrogen blends.

2. Methodology

2.1. Experimental set-up

A tangential swirl burner, with a geometric swirl number of $S_g = 1.05$ was employed at different thermal powers and Reynolds numbers (Re) as shown in Fig. 1. The burner was supplied using Bronkhorst mass flow controllers ($\pm 0.5\%$ within a range of 15–95% mass flow). The unit was fed using ammonia and hydrogen as shown in Table 1. Ammonia and air were injected at the mixing chamber, while hydrogen was injected through 6 equispaced holes, located 4 cm below the burner exit, angled at 45° , directly into the swirler for premixing with ammonia and air. Various conditions were assessed to determine the impact of ammonia mole fraction on N_2O formation at a constant equivalence ratio, $\Phi = 0.65$.

Experiments were conducted at atmospheric pressure (1.1 bara) and inlet temperature (288 K). A pair of LaVision CCD cameras were employed to obtain line-of-sight chemiluminescence traces of various species. The units were triggered simultaneously at a frequency of 10 Hz with constant gain. A range of optical (Edmond) filters were used for each species of interest, namely OH^* (309 nm; $A^2\Sigma^+ - X^2\Pi$ system) [32], NH^* (336 nm; $A^3\Pi - X^2\Sigma^-$ system) [32–35] and NH_2^* (630 nm; single peak of the NH_2 α band) [32,36]. LaVision Davis v10 was used to gather 500 frames for each data point, which were then temporally averaged, and post-processed using a bespoke MatLab script [37] designed to conduct Abel Deconvolution with the assumption of flame symmetry, following a 3×3 pixel median filter, as per [38–40]. Colourmaps of the chemiluminescence images have been normalised to the maximum intensity of each image to display the changes in species distributions for each flame.

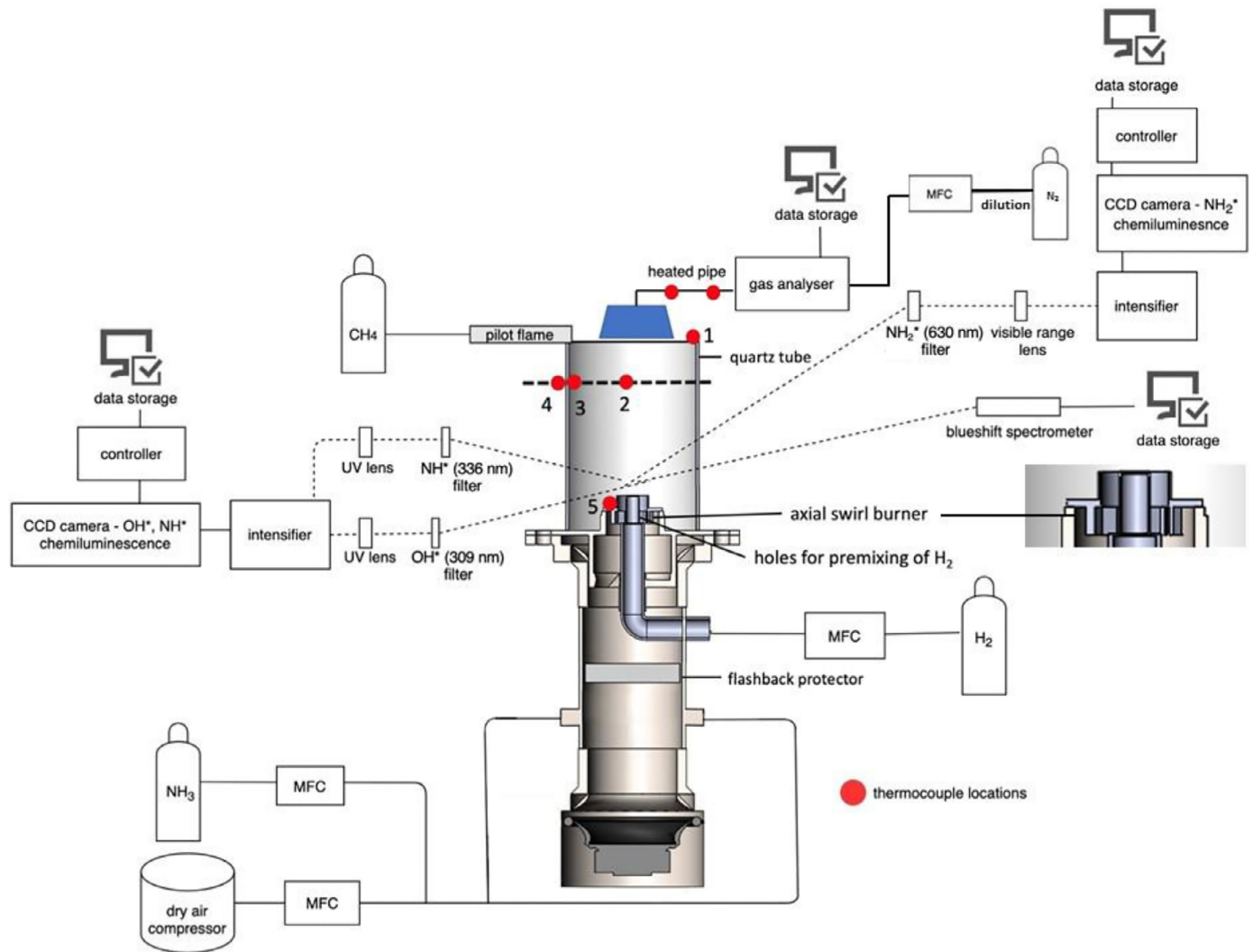


Fig. 1. Tangential combustor with measuring techniques and control systems.

Table 1
Experimental matrix.

Parameter	Value	Parameter	Value
Blends NH_3/H_2 (vol%)	50/50 – 90/10 (steps of $\pm 5\%$)	Inlet Temperature	288 K
Thermal Power (bulk gas velocity)	10 kW (26.9–27.3 m/s), 15 kW (40.3–41 m/s) and 20 kW (53.7–54.6 m/s)	Inlet Pressure	0.11 MPa
Reynolds No. (bulk gas velocity)	20,000 (21.4–19.9 m/s), 30,000 (32.1–29.8 m/s) and 40,000 (42.9–39.8 m/s)	Outlet Pressure	0.10 MPa
Equivalence Ratio (Φ)	0.65	Swirl	1.05

Temperature profiles were obtained via K and R type thermocouples feeding a data logger with a frequency of 1 Hz. Thermocouple data were taken for 120 s for each point and averaged. The thermocouples were calibrated showing an average error of 3% of reading. The acquired temperature data were corrected as per [41] to account for the convective and radiative heat transfer of the thermocouples with their surroundings, as well as conductive heat transfer between the thermocouple bead and the connecting thermocouple wires. Exhaust emissions (NO , N_2O , NO_2 , NH_3 , O_2 and H_2O) were measured using a bespoke Emerson CT5100 Quantum Cascade Laser analyser at a frequency of 1 Hz, a repeatability of $\pm 1\%$, 0.999 linearity, and sampling temperature up to 190 °C. A heated line at 160 °C was employed to avoid condensation and capture exhaust samples. Dilution methodology was introduced by

adding N_2 in the sample using high precision Bronkhorst EL-FLOW Prestige MFC. The N_2 then get heated up to 160 °C by the system prior to mixing with the exhaust samples. The flowmeter of the analyser is calibrated by the manufacturer and this is enough for its usual purpose. The flow rate of the exhaust process sample in the system during dilution methodology is then calculated by Eq. (1).

$$\text{Exhaust sample flowrate } (F_5) = \text{Total intake flowrate } (F_i) - \text{Dilution } (\text{N}_2) \text{ flowrate } (F_d) \quad (1)$$

This dilution methodology has a repeatability of $\pm 10\%$, applied when wet readings were above the analyser's detection range. An isokinetic funnel with an intake diameter of 30 mm was fixed at 50 mm above the quartz exit to capture homogeneous samples at

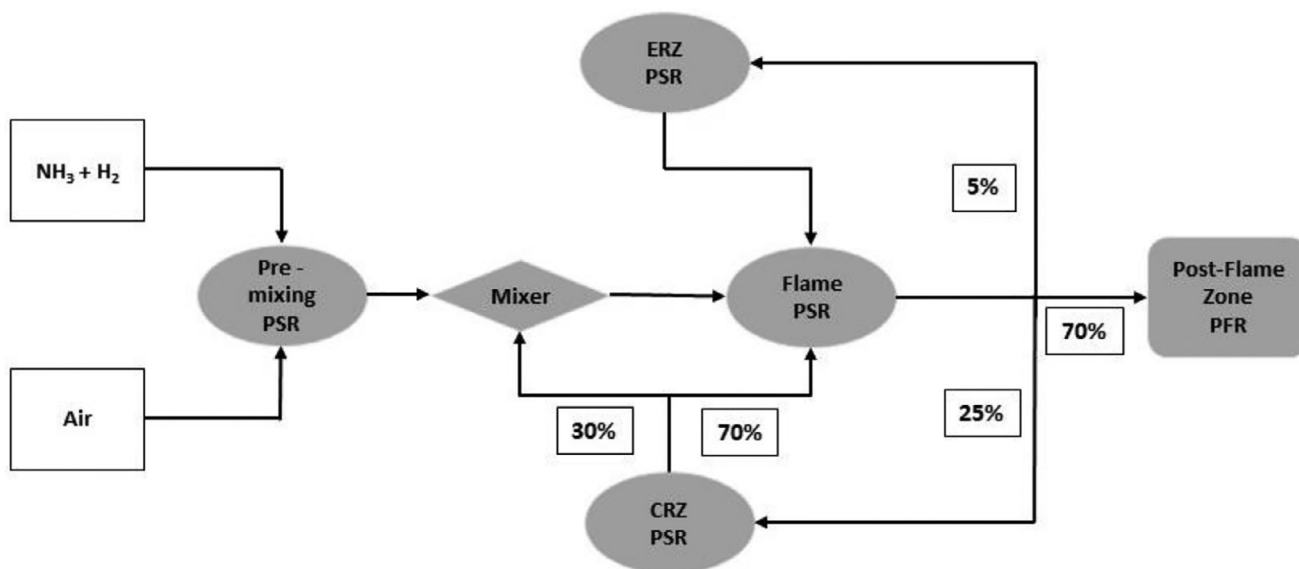
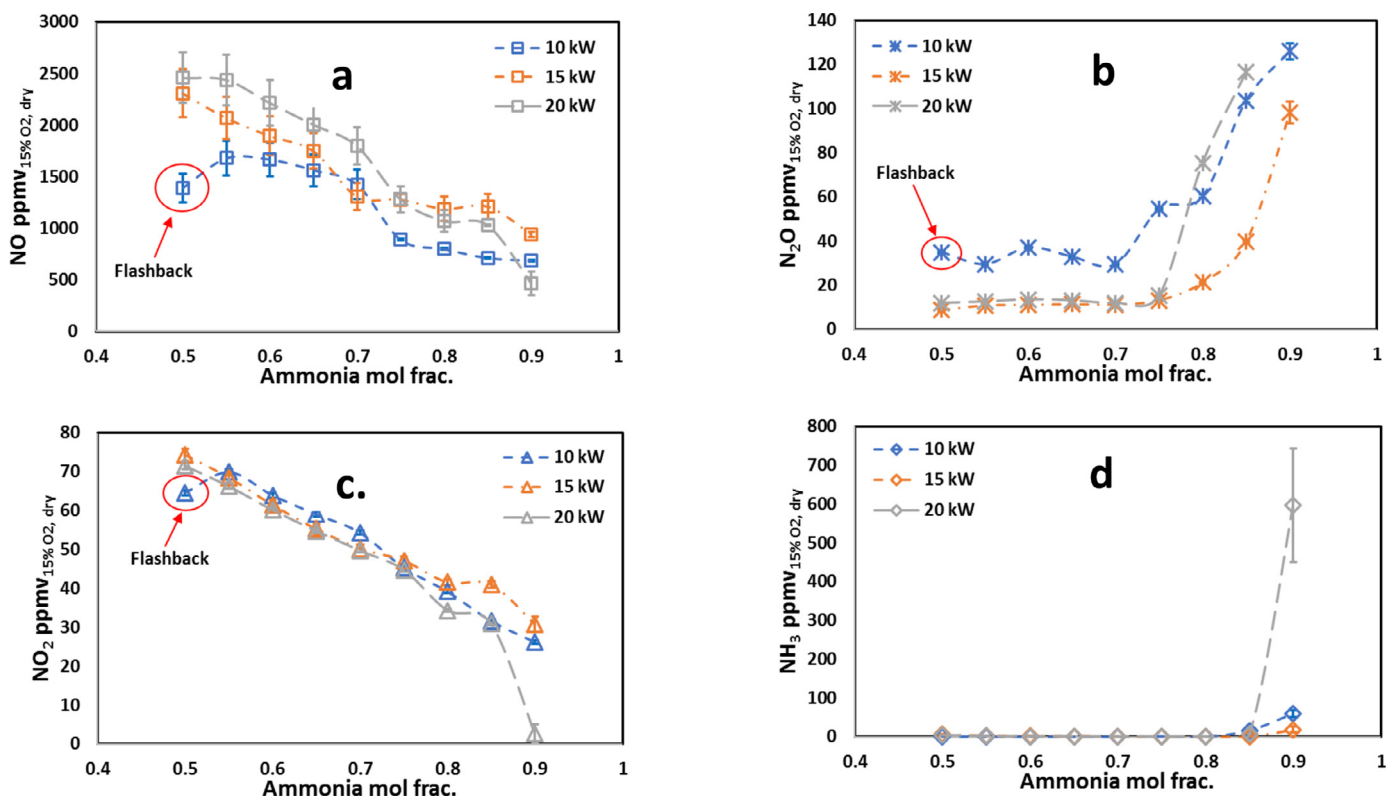


Fig. 2. Chemical reactor network (CRN).

Fig. 3. Sampled NO (a), N₂O (b), NO₂ (c) and NH₃ (d) emissions at different thermal powers and $\Phi = 0.65$.

the exhaust for all test points. All the emissions data reported here were taken over a period of 120 s and averaged for each condition. All the emissions data presented in Fig. 3 are normalised to 15% O_2 [42]. A Logitech C270 camera was used to monitor the flame stability at a distance of 5 m. Finally, a Blue-Wave StellarNet CMOS spectrometer with a detector ranging from 200 to 1100 nm was focused on the flame core. An embedded software (SpectraWiz) was used to record the spectrographic signatures of all flames.

2.2. Chemical kinetic modelling

A chemical reactor network (CRN), previously developed elsewhere [37,43,45], was employed to model the combustion zone, as shown in Fig. 2. Mixing zones, flame zones, central recirculation zone (CRZ) and external recirculation zone (ERZ) were modelled by individual perfectly stirred reactors (PSR) and the volume and/or residence time for each PSR were obtained from previous RANS CFD analysis [46]. The recirculation strength was determined

by previous experimental campaigns that employed comparable industrial scale swirl burners [37,45,47]. The post-flame zone (PFZ) was modelled by a plug flow reactor (PFR) with one dimensional length of 15 cm. Approximation of the heat loss values was derived experimentally from the corrected thermocouple measurements. The background physics and rationale in the development of this network are detailed in [37] and summarised in the supplementary material, Section 1. Similar to our recent work [45], numerical calculations were carried out to estimate the change in volumes for flame zone, CRZ and ERZ PSRs for all conditions considered here. These approximated values are detailed in the supplementary material, Table S.2 – S.7.

To evaluate the contribution of elementary reactions to the formation and consumption of N_2O , absolute ROP values were used for flame zone as 0-D PSR was used to model the flame zone and integrated values of the production rate, I_R , were evaluated for PFZ, as defined in Eq. (2),

$$I_R = \int_0^L \dot{\omega}_{R,i} dX \quad (2)$$

where $\dot{\omega}_{R,i}$ is the rate of production of the species, i , through the reaction, R . The length of the integration domain, L , was set to 15 cm, as per the defined length of PFZ.

3. Results

3.1. Constant thermal powers

Sampled concentrations of NO, N_2O , NO_2 and NH_3 at different thermal powers are shown in Fig. 3. Overall, NO and NO_2 emissions decrease with increasing ammonia content while N_2O emissions increase. NH_3 emissions are negligible for up to 80% vol NH_3 fuel blends. Flashback was observed in low power 50/50_{VOL.%} NH_3/H_2 blend due to increased flame speed compared to lower gas speed, as a result of increased hydrogen content in the blend [5,27]. It must be noted that NO_x emissions were negligible for 100% CH_4 case with $\Phi = 0.65$ at different thermal powers and CO_2 emissions were around $\sim 7\%$ at these powers. More NH_3 content in the fuel led to an increase of NH_2^* production at the flame, as evidenced by the chemiluminescence images in Fig. 4 for 20 kW NH_3/H_2 blends. The figure shows that areas with higher intensity has increased NH_3 content. Note that the origin corresponds to the burner centreline. Measured NH_2^* intensities were found to be significantly higher than OH^* and NH^* intensities across all flames, with NH^* being the lowest amongst the three species. Even though the proportionality between ground state species and electronically excited species is complicated due to various effects such as quenching and radiation losses, previous work [48] has assumed proportionality between ground state and electronically excited species in NH_3 disassociation processes. In this study, a similar positive correlation between ground state and emitting species has been applied [35,40,49,50].

Chemiluminescence spectra of 20 kW NH_3/H_2 flames at $\Phi = 0.65$ is shown in Fig. 5. OH^* and NH^* signatures decrease with increasing NH_3 mole fraction in the flame. However, the intensity of NH_2^* signatures at ~ 632 nm for up to 70% NH_3 are nearly constant and decreasing afterward with increasing ammonia content in the fuel blends, Fig. 5. This behaviour of NH_2^* can be attributed to an increase of temperature at the flame due to the low NH_3 content in the flame. Recent studies [40,45] have highlighted the importance of NH_2 radicals in NH_3/H_2 blends as a heat release marker. Thermocouple measurements showed markedly high temperatures at different locations in the presence of high H_2 content, 1257 K at 50% H_2 and 1185 K at 15% H_2 at 20 kW, measured at 3.9 cm below the quartz exit. Simultaneously, the area of radical formation increases significantly with increasing NH_3 content in the fuel, Fig. 4, which is in line with increased flame thickness ob-

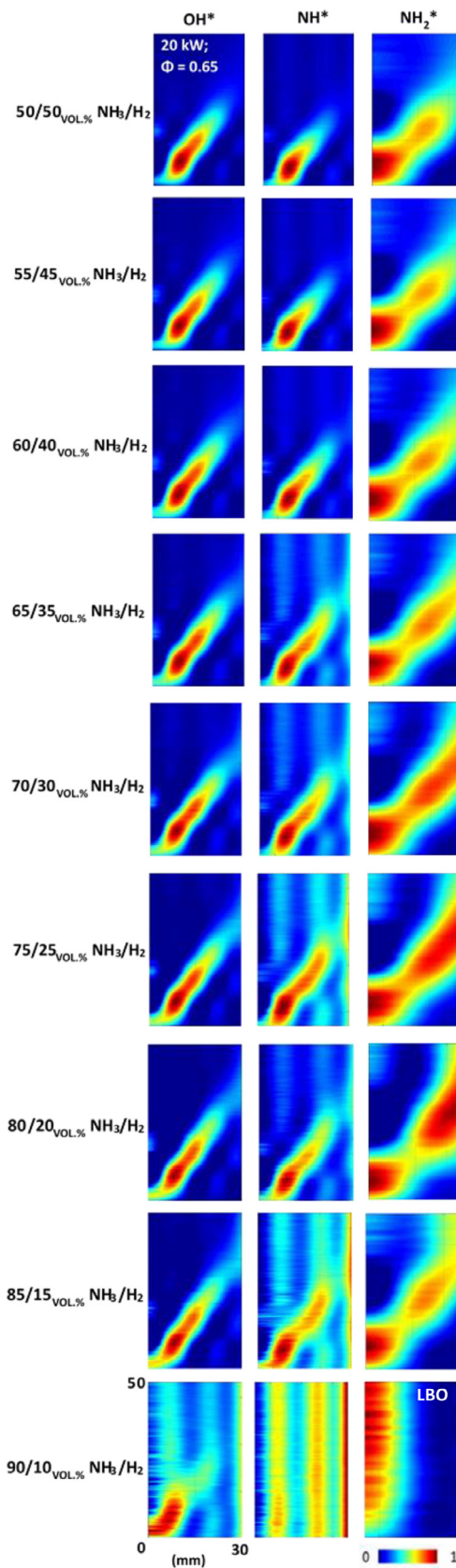


Fig. 4. Abel transformed OH^* , NH^* and NH_2^* chemiluminescence for 20 kW thermal power and $\Phi = 0.65$. Colourmap normalised to image dataset max.

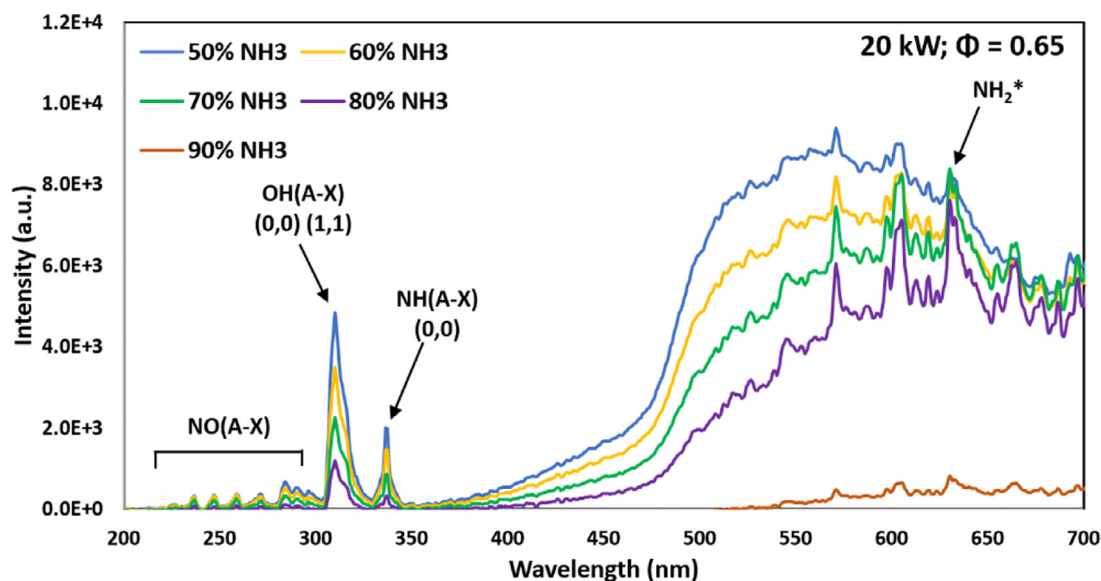


Fig. 5. Chemiluminescence spectrum of 20 kW NH_3/H_2 flames at $\Phi = 0.65$.

served in ammonia blended fuels [13,14,51]. Necking observed in the chemiluminescence images reported in Fig. 4 can be attributed to the Abel-Deconvolution routine. The scale of necking is highly dependant on available signals, thus mostly visible in NH_2^* images. Our earlier study [52] in CH_4/NH_3 flames indicated high NH_2^* occurrence further downstream from the mean location of NH^* and in opposite trends. However, in the current study of NH_3/H_2 flames under lean condition, NH_2^* formations are found to be centred at burner exit at high concentrations for all conditions and spreads closer to burner wall as ammonia content in the fuel blends increases up to 80%, whilst NH^* formed within the core of the flame. The NH_2^* and NH^* profiles overlap with each other, but the former covers larger area. This observation can be attributed to the rate of consumption of the radicals. High NH_2^* signal was recorded in the regions where OH^* intensity was minimum, suggesting the production of NH_2 in regions where a high consumption rate of NH_3 by reacting with OH radicals is not guaranteed. Meanwhile, NH^* production increases at the core of the flame due to enhanced reactivity and frequent collisions in this region, as well as the presence of concentrated OH^* radicals, thus converting NH_2 radicals to NH radicals. As the OH^* and NH^* profiles perfectly overlap each other, the presence of high OH concentrations at regions of high NH concentrations ensures fast NH oxidation, making its profile relatively smaller than that of NH_2 . Further investigations are recommended utilising Planar Laser Induced Fluorescence (PLIF) technique to better understand the reactivity of these radicals.

Decreasing NO formation with increasing NH_3 concentration can be attributed to increased NH_2 production at the tip of the flames, Fig. 4, which has been identified as the key species for NO consumption in the flame through the chain branching reaction $\text{NH}_2 + \text{NO} \leftrightarrow \text{NNH} + \text{OH}$ and the chain terminating reaction $\text{NH}_2 + \text{NO} \leftrightarrow \text{H}_2\text{O} + \text{N}_2$ [43,53]. Major sources of NO production in NH_3 flames are through HNO via reaction with oxygen molecules and hydrogen radicals. However, HNO is mainly produced in the ammonia flames through the combination reaction $\text{NH} + \text{OH} \leftrightarrow \text{HNO} + \text{H}$ [43,45]. As per Fig. 5, OH^* and NH^* intensity decrease with increasing ammonia portion in the fuel, which reflects the reduction of NO production, Fig. 3(a) [22,54]. Significant amount of NH_2 also reacts with O radicals to produce HNO but the avail-

ability of O radicals which are mainly produced through $\text{O}_2 + \text{H} \leftrightarrow \text{O} + \text{OH}$ decreases with decreasing H_2 percentage in the flame which restricts H radicals production.

N_2O is mainly produced in ammonia flames through the reaction $\text{NH} + \text{NO} \leftrightarrow \text{N}_2\text{O} + \text{H}$ and it is reduced to N_2 by reacting with H and via the third body reaction $\text{N}_2\text{O} + \text{M} \leftrightarrow \text{N}_2 + \text{O} + \text{M}$ [27,55,56]. These reactions explain the observed increasing trend of N_2O production with decreasing NO production as NO is not being converted to N_2O due to decrease in NH production, as well as reduced N_2O consumptions through the third body reaction at low temperatures, an assumption that is in line with the observed NH trends of Fig. 4. At the flame zone with the availability of H radicals, specially at high H_2 fuel blends, N_2O reduces to N_2 through the reaction $\text{N}_2\text{O} + \text{H} \leftrightarrow \text{N}_2 + \text{OH}$. Moreover, the observed rapid increase in N_2O emissions at $\geq 80\%$ NH_3 blends, may be due to the effects of liner wall heat loss on the flame as also observed by Okafor et al. [25]. Fig. 6 shows the changes in liner wall temperature measured at 3.9 cm below the liner exit (post flame zone) using thermocouples. Increases in the difference in wall temperatures at the post flame zone are observed for 80% and above NH_3 blends at all thermal power conditions, which reflects into higher heat losses at the flame zone, thereby higher N_2O productions. Simultaneously, with increasing ammonia contents in the blends, ammonia chemistry becomes more dominant in the flame and responds more to heat loss [57]. Flame speed also decreases with increasing ammonia content; hence the chemical time scale increases relative to the fluid residence time, encouraging N_2O emissions as evident by Fig. 3(b).

Further analyses show that NO converts to NO_2 by reacting with HO_2 and through the third body reaction $\text{NO} + \text{O} + \text{M} \leftrightarrow \text{NO}_2 + \text{M}$ [43,44]. Most of this NO_2 reverts to NO by reacting with O and H radicals. Measured NO_2 for the thermal power conditions decreases monotonically as NH_3 content in the fuel increases. This trend is a by-product of ammonia's deNOx capability which reduces NO production and thereby NO_2 production. NH_3 emissions at the exhaust are nearly zero up to 80% ammonia, due to high hydrogen content as H_2 enhances OH production, thus converting NH_3 to NH_2 radicals. Above 80% ammonia content in the fuel blends, especially at 90% ammonia blends, NH_3 slip increases

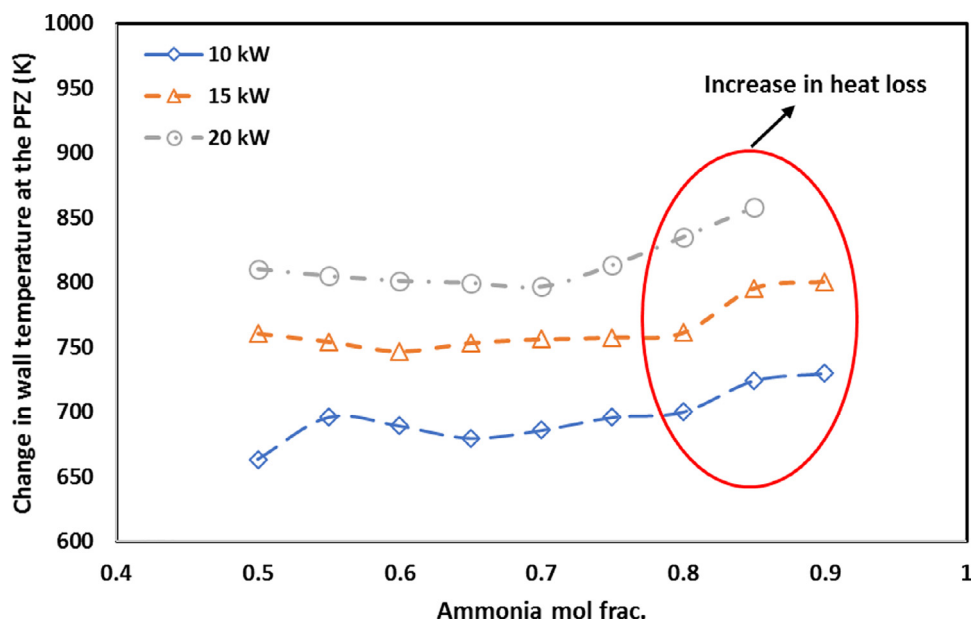


Fig. 6. Change in wall temperatures at different thermal power conditions.

due to the decrease in flame speed, moving towards lean blow off (LBO) scenarios, Fig. 4.

An interesting pattern was observed when analysing NO emissions, Fig. 3(a), which show overlaps between different thermal powers for $X_{\text{NH}_3} \geq 0.8$. These discrepancies can be explained through the various radical formation under these conditions. Fig. 7 shows the Abel-deconvoluted radical chemiluminescence at 85/15_{VOL%} NH₃/H₂ blend at different thermal power and Fig. 8 shows the radical spectroscopic signature. These figures denote maximum radical intensities at 15 kW which reflect the maximum NO production as NH₂ converts to NH by reacting with OH radicals whilst NH and OH combine to produce HNO, species responsible for most NO formation. The decrease in NO reading at 90/10_{VOL%} NH₃/H₂ fuel at 20 kW is due to the LBO scenario, keeping most of the fuel remaining unburnt, Fig. 3(d). Furthermore, in a recent work by Manna et al. [58], it was shown that hydrogen only moderately enhances the reactivity of the system at low H₂ concentration blends (up to 15%) and low temperature (1200 K – 1350 K) combustion processes. Therefore, dynamic regime areas are restricted to a narrower Φ range, depicted by the LBO scenario observed in this study.

3.2. Constant Reynolds numbers

Many practical systems utilise constant Re number scenarios for power generation and comparison purposes between rigs [59,60]. Hence, three Re (20,000, 30,000 and 40,000) scenarios were also considered in this section at a fixed $\Phi = 0.65$ to analyse the effect of turbulence on flame characteristics and emissions. Bulk gas velocities at a constant Re decrease with increasing X_{NH_3} , opposed to the increasing velocity trend at constant thermal powers (Table 1). Sampled emissions are displayed in Fig. 9. 50/50_{VOL%} NH₃/H₂ blends at $Re = 20,000$ suffered from flashback as it did for 10 kW thermal power due to the high H₂ content in the fuel. NO emissions at the exhaust for $Re = 20,000$ are about 2.5 – 3 times lower than for the other two Reynolds number conditions up to $X_{\text{NH}_3} = 0.7$, a phenomenon caused by the lower reactivity and radical formation at $Re = 20,000$ (as observed in the

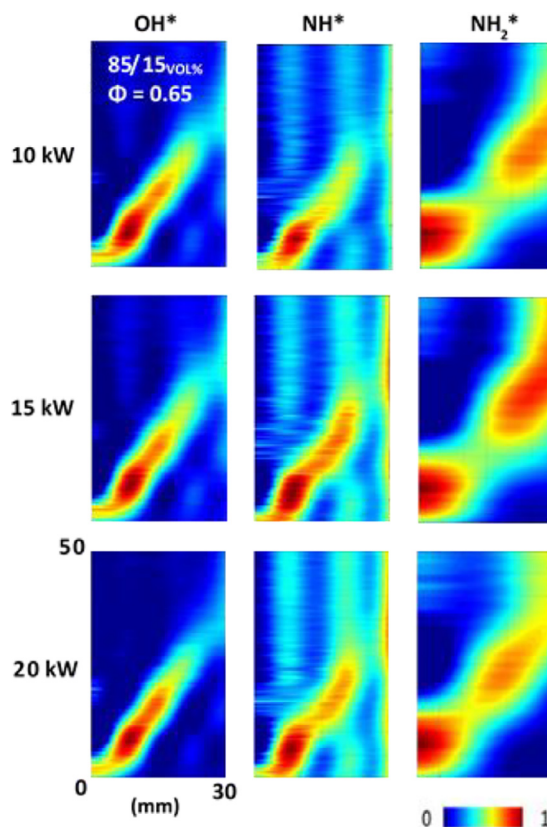


Fig. 7. Abel transformed OH*, NH* and NH₂* chemiluminescence for 85/15_{VOL%} NH₃/H₂ blends at different thermal powers and $\Phi = 0.65$. Colourmap normalised to image dataset max. .

chemiluminescence spectrums shown in Fig. 10). NO* signature in Fig. 11 also displays similar trends as the measured emissions at exhaust. For 80% and more NH₃ content in the fuel, NO production in the flame for all Reynolds number conditions are clustered to-

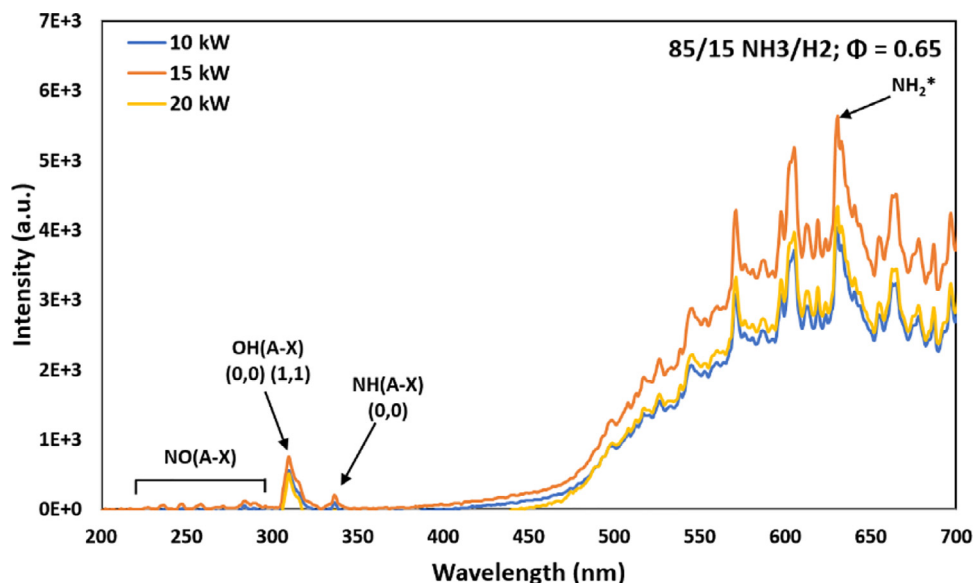


Fig. 8. Chemiluminescence spectrum of 85/15_{VOL%} NH₃/H₂ flames at different thermal powers and $\Phi = 0.65$.

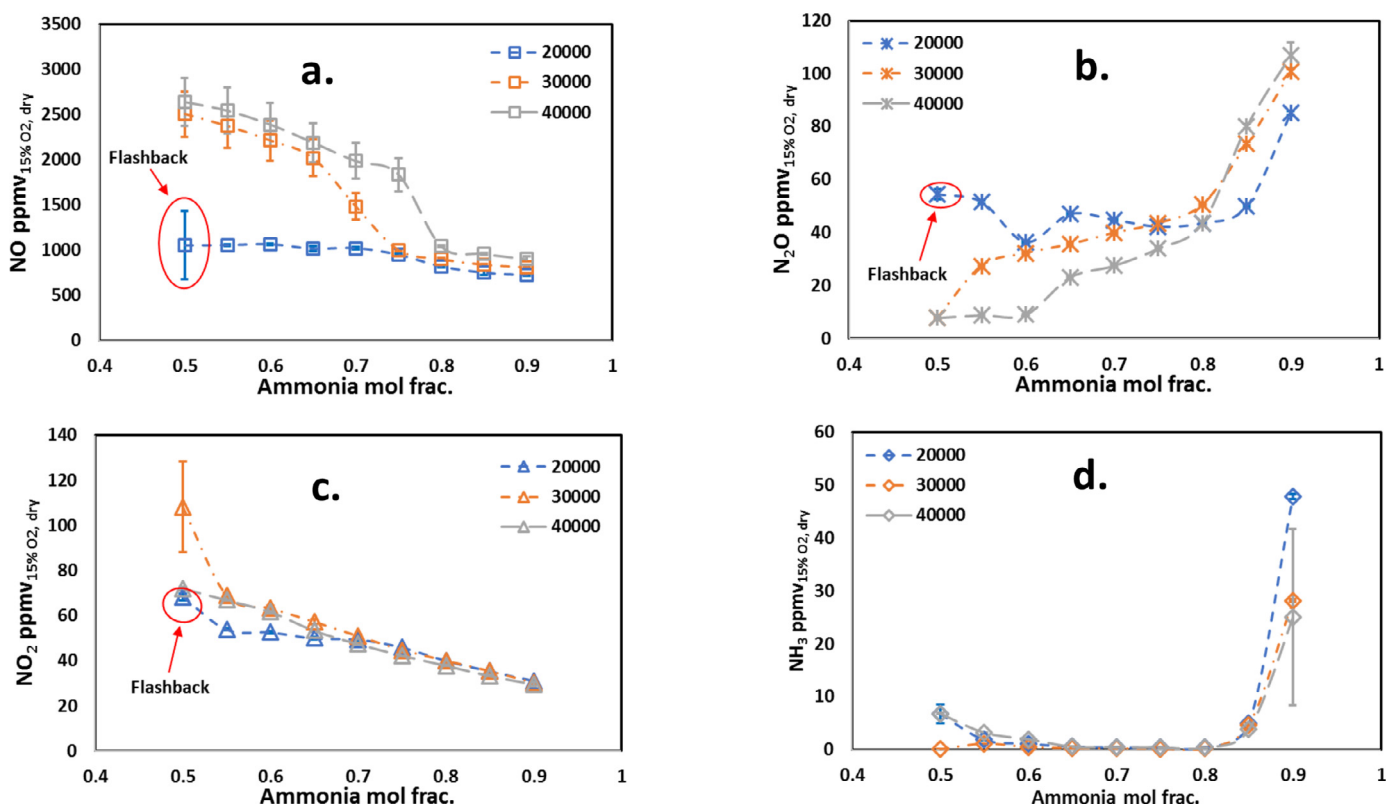


Fig. 9. Sampled NO (a), N₂O (b), NO₂ (c) and NH₃ (d) emissions at different Reynolds numbers and $\Phi = 0.65$.

gether as the radicals of interest have similar intensities at these ranges, Fig. 11.

Fig. 11 shows the Abel-deconvoluted OH*, NH* and NH₂* chemiluminescence images at $Re = 40,000$ and $\Phi = 0.65$. Colourmap of the images are normalised to image dataset maximum to show the change in topology for changing fuel blend. Even

though NH₂* radicals cover more area in the flame with increasing X_{NH_3} , intensity of the NH₂* radicals follow opposite trends, as evidenced by Fig. 10(c). NH* and OH* distributions seem to be closely matching each other as these radicals are related by the reaction $NH_2 + OH \leftrightarrow NH + H_2O$, which is also the largest route of NH production from NH₂. NH radicals eventually convert to N₂O by con-

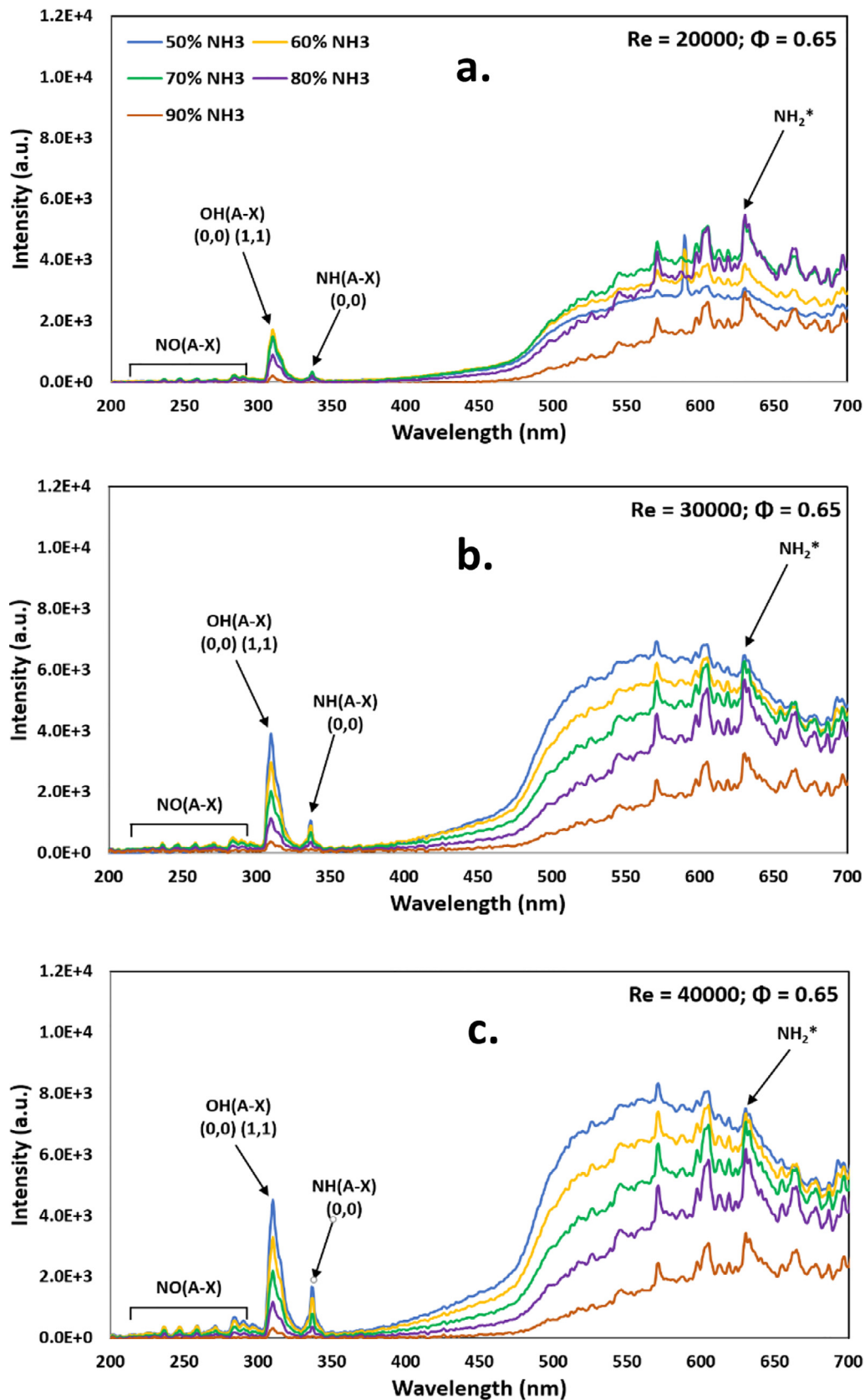


Fig. 10. Chemiluminescence spectrum of $Re = 20,000$ (a); $Re = 30,000$ (b) and $Re = 40,000$ (c) NH_3/H_2 flames at $\Phi = 0.65$.

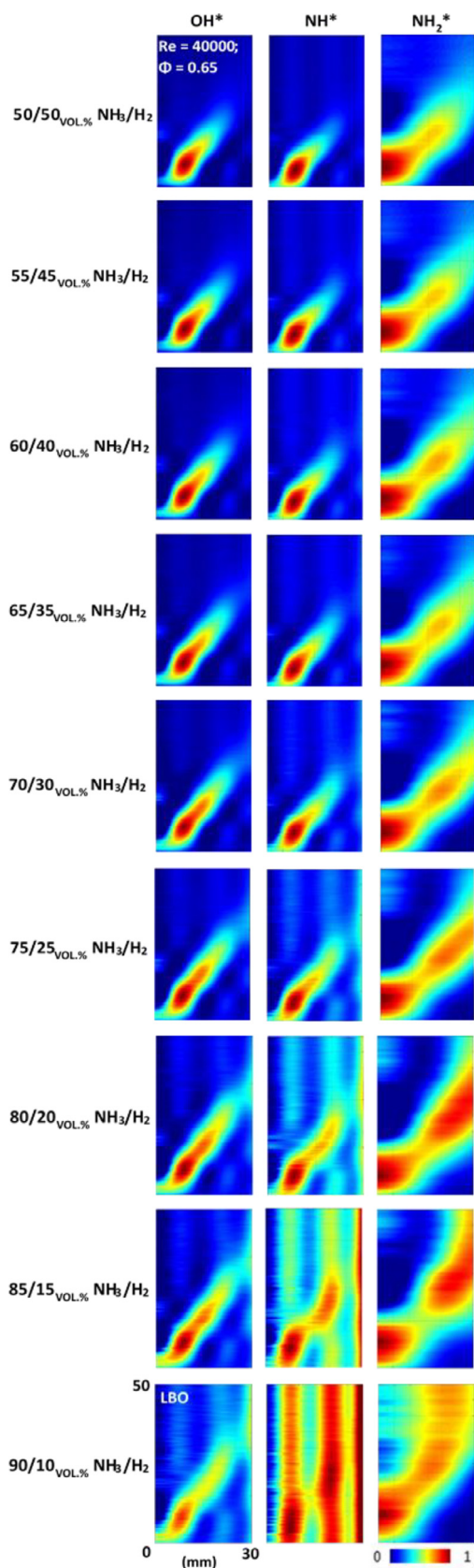


Fig. 11. Abel transformed OH^* , NH^* and NH_2^* chemiluminescence for $Re = 40,000$ and $\Phi = 0.65$. Colourmap normalised to image dataset max.

suming NO as mentioned earlier. Therefore, measured N_2O emissions follow opposite trends compared to NO emissions across different Reynolds number conditions. Beyond 80% NH_3 blends N_2O production increases sharply as was seen with the constant thermal power cases. This again can be attributed to increased heat losses as well as decreased presence of H_2 in the flame, which reduces H radical production, thereby restricting N_2O consumption through the reaction $\text{N}_2\text{O} + \text{H} \leftrightarrow \text{N}_2 + \text{OH}$. N_2O formation at different fuel blends will be discussed in more detail at the latter part of this study. NO_2 emissions at different Reynolds numbers display similar characteristics as those at various thermal power conditions. However, the 30,000 Re case displays high NO_2 emissions at 50/50_{VOL%} blend but barring that, all the other measured values are almost clustered together. High NH_3 slip are observed at $X_{\text{NH}_3} = 0.9$ as the flame nears LBO.

3.3. Numerical simulation

Numerical simulations were carried out based on the experimental conditions, Table 1. Initial analyses were conducted using the proposed CRN, Fig. 2, to determine the mechanism that would be employed for detailed N_2O sensitivity analyses. Reaction mechanisms from Okafor et al. [13], Glarborg et al. [61], Otomo et al. [62], Xiao et al. [29], Stagni et al. [56], and Tian et al. [63] were utilised to predict species formation through the system and compare with the experimental data. Figs. 12 and 13 show the comparison between wet experimental results and mechanisms predictions for 15 kW thermal power and $Re = 40,000$, respectively. Other thermal power and Reynolds number comparisons are given in the supplementary material, Fig. S.3 – S.6. It must be noted that even though predictions for NO_2 showed similar experimental trends, all the mechanisms predicted 2–3 times lower values than their experimental counterparts. As this study is focused on N_2O formation in NH_3/H_2 flames, NO_2 predictions were not included in this study. However, this is a point that requires further development out of the scope of this work.

Comparison between experimental results and mechanisms predictions for NO (a) and N_2O (b) at 15 kW thermal power with fixed $\Phi = 0.65$.

Predictions by all the mechanisms considered here follow overall experimental trends of NO and N_2O formation. While most of the mechanisms predict N_2O experimental results closely, Stagni mechanism's predictions were very close to N_2O productions and also was the closest predictor of NO emissions with the employed CRN model. Therefore, Stagni mechanism was chosen to conduct [N_2O] sensitivity analysis detailed in the next section.

3.3. [N_2O] sensitivity analysis

Sensitivity analyses of N_2O concentration for 50/50_{VOL%}, 70/30_{VOL%}, and 90/10_{VOL%} NH_3/H_2 blends at 15 kW and $Re = 30,000$ has been carried out in addition to analysis of the quantitative reaction path diagrams (QRPD), constructed based on rate of production (ROP) of species, Figs. 14–19.

Fig. 14 shows the QRPD for NO_x production and consumption at the flame zone for the three NH_3/H_2 blends at 15 kW under consideration here. NH_3 reacts with OH radicals and converts to NH_2 radicals to start the process of NH_3 oxidation at the flame zone. NH_2 then reacts with OH and O radicals to produce NH and HNO , respectively. NH_2 also consumes NO to produce N_2 and NNH radicals through the chain terminating and branching reactions, respectively, as discussed earlier. NH radicals then convert to NO directly by reacting with atomic and molecular oxygen, producing H and OH radicals, respectively as by-products. NH radicals are also responsible for further NO formation via HNO and atomic N production. Nitroxyl (HNO) is the major source of NO formation at the

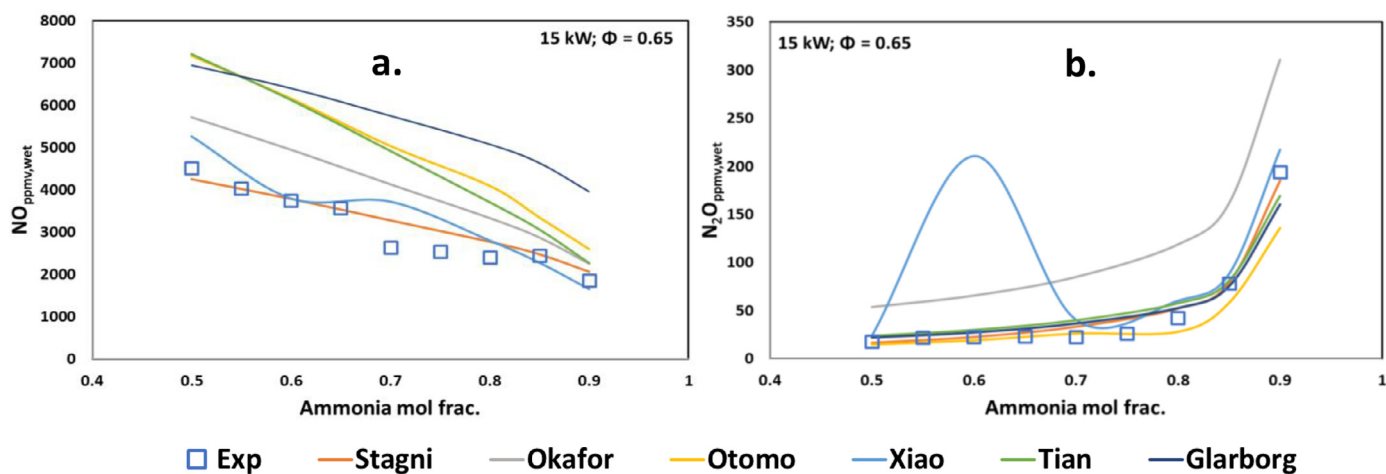


Fig. 12. Comparison between experimental results and mechanisms predictions for NO (a) and N_2O (b) at 15 kW thermal power with fixed $\Phi = 0.65$.

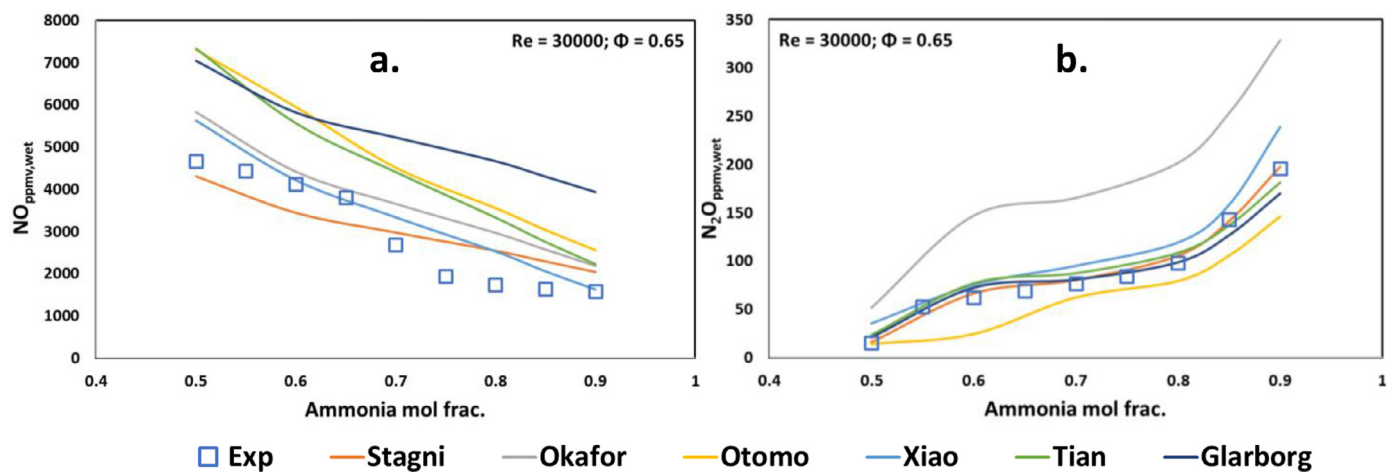


Fig. 13. Comparison between experimental results and mechanisms predictions for NO (a) and N_2O (b) at $Re = 30,000$ with fixed $\Phi = 0.65$.

flame zone through the reactions with molecular oxygen, H and O radicals. Atomic N also reacts with molecular O_2 and OH radicals to produce NO. Other than the reaction with NH_2 , NO also reacts with N and NH to produce stable molecular nitrogen. NH and NO combine together to produce N_2O through the reaction $NH + NO \leftrightarrow N_2O + H$ (R1). Finally, N_2O converts to N_2 through the reactions $N_2O + H \leftrightarrow N_2 + OH$ (R2) and $N_2O(+M) \leftrightarrow N_2 + O(+M)$ (R3). From Fig. 14, reaction rates for the same reactions increase as X_{NH_3} increases from 0.5 to 0.7 but then reduces at 90% NH_3 due to severe decrease of H_2 content in the flame, affecting the production of important radicals (H, O and OH) as well as the flame stability, evidenced in Figs. 4 and 11.

Figs. 15 and 16 detail the computed normalised sensitivity and absolute ROP of $[N_2O]$ at the flame zone for different fuel blends at 15 kW and $Re = 30,000$, respectively for constant $\Phi = 0.65$. Reaction R2 has the most negative sensitivity for both 15 kW and $Re = 30,000$ across all the three blends which reflects in the ROP diagrams. ROPs for reaction R2 decreases with increasing ammonia contents for various Reynolds number conditions as expected due to decreased availability of H radicals, but interestingly, increases for the 70/30 blend at 15 kW, followed by a de-

crease with the 90/10 blend. This can be attributed to the predicted temperature at the flame zone by the Stagni mechanism. The 70% NH_3 blend shows a slight increase in temperature at 15 kW (1655, 1656 and 1622 K at $X_{NH_3} = 0.5, 0.7$ and 0.9, respectively), compared to a decrease suffered at $Re = 30,000$ condition (1655, 1635 and 1621 K at $X_{NH_3} = 0.5, 0.7$ and 0.9, respectively). The reaction R1, which has the reactants of reaction R2 as the products follows the similar trend. The third body reaction R3 is the second most important reaction for consumption of N_2O at the flame zone.

Numerical analyses showed substantial amounts of N_2O reduction at the post flame zone for both thermal power and Reynolds number conditions. Normalised sensitivity coefficients and integrated ROP values for $[N_2O]$ at the post flame zone are reported in Figs. 17 and 18 for different fuel blends at 15 kW and $Re = 30,000$, respectively. It must be noted the sensitivity graphs are taken at 13 cm from the burner exit as this distance was most representative to the experimental system, as well as most representative across 15 cm PFR distance considered here. However, the ROP graphs report integrated rate of productions across the post flame zone, as per Eqn 2. At the post flame zone, reaction R3 becomes

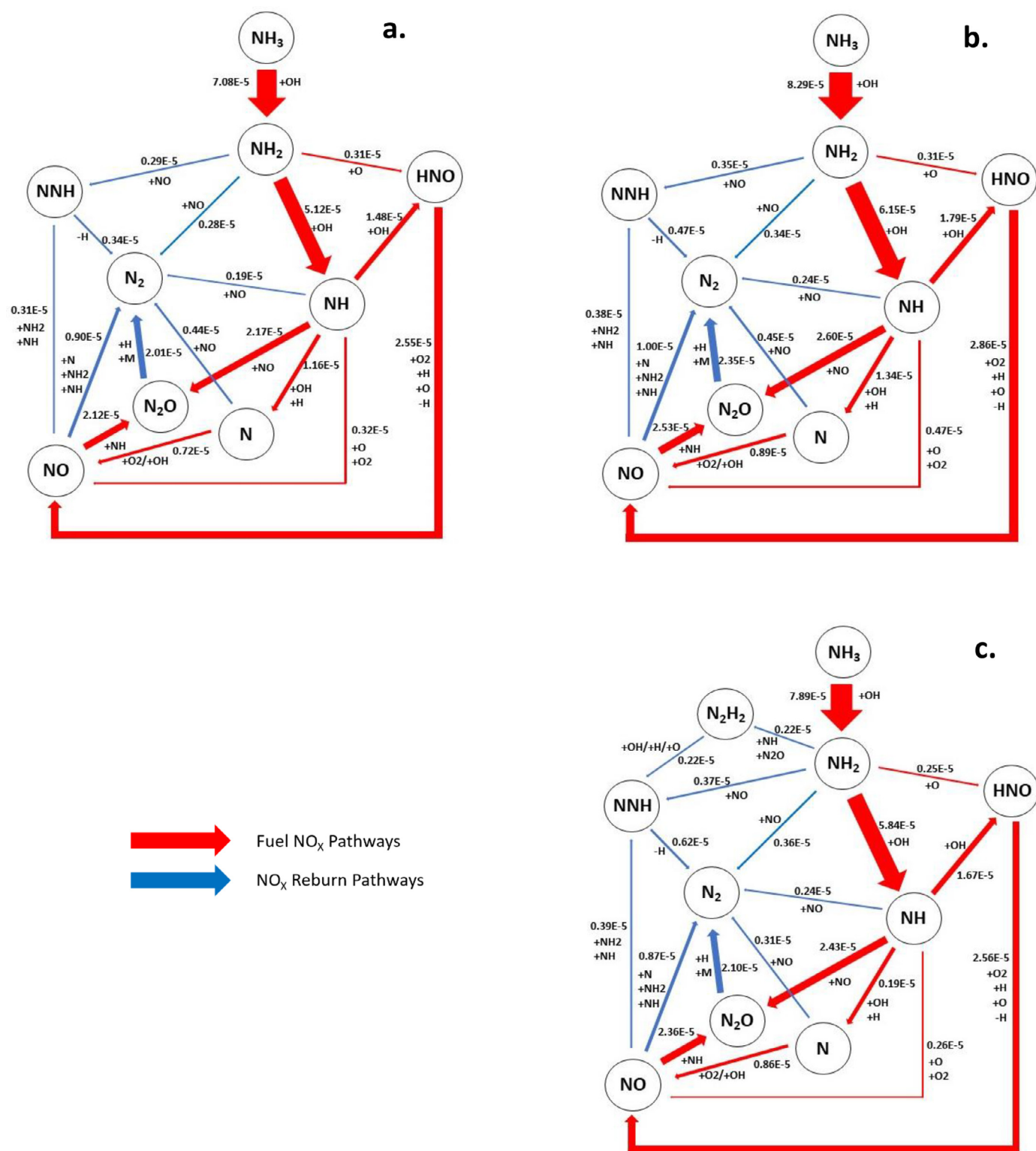


Fig. 14. Quantitative reaction path diagram showing NO_x formation/reburn pathways at the flame zone for 50/50_{VOL%} (a); 70/30_{VOL%} (b) and 90/10_{VOL%} (c) NH₃/H₂ blends at 15 kW and fixed $\Phi = 0.65$. Unit - mole/cm³-sec.

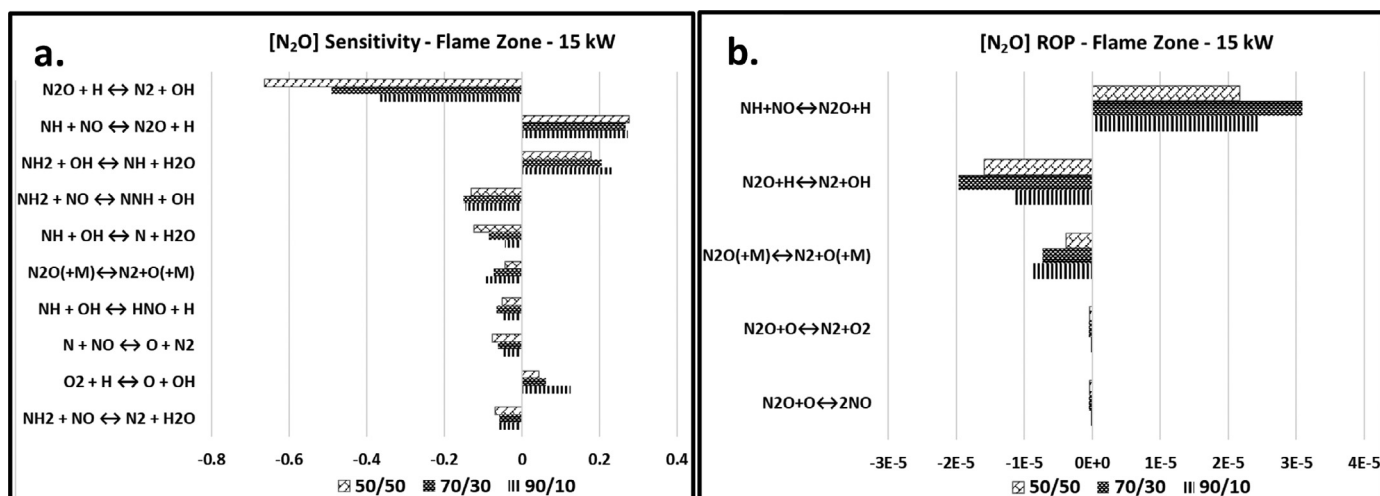


Fig. 15. Normalised sensitivity coefficients (a), and absolute ROP (b) of $[N_2O]$ at the flame zone for 15 kW and fixed $\Phi = 0.65$. Unit of absolute ROP – mole/cm³-sec.

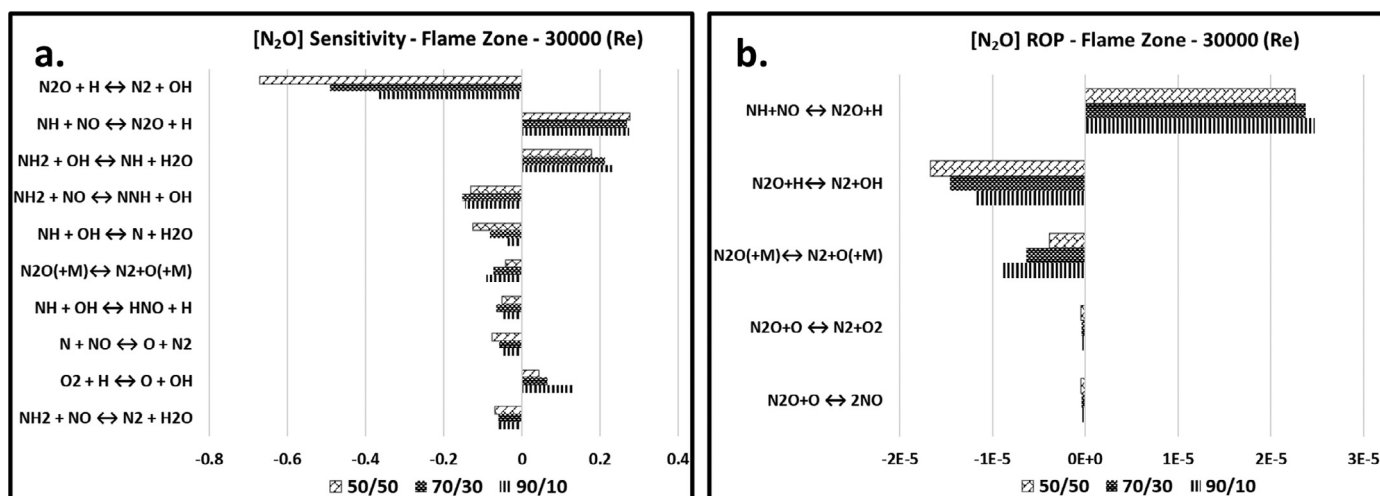


Fig. 16. Normalised sensitivity coefficients (a), and absolute ROP (b) of $[N_2O]$ at the flame zone for $Re = 30,000$ and fixed $\Phi = 0.65$. Unit of absolute ROP – mole/cm³-sec.

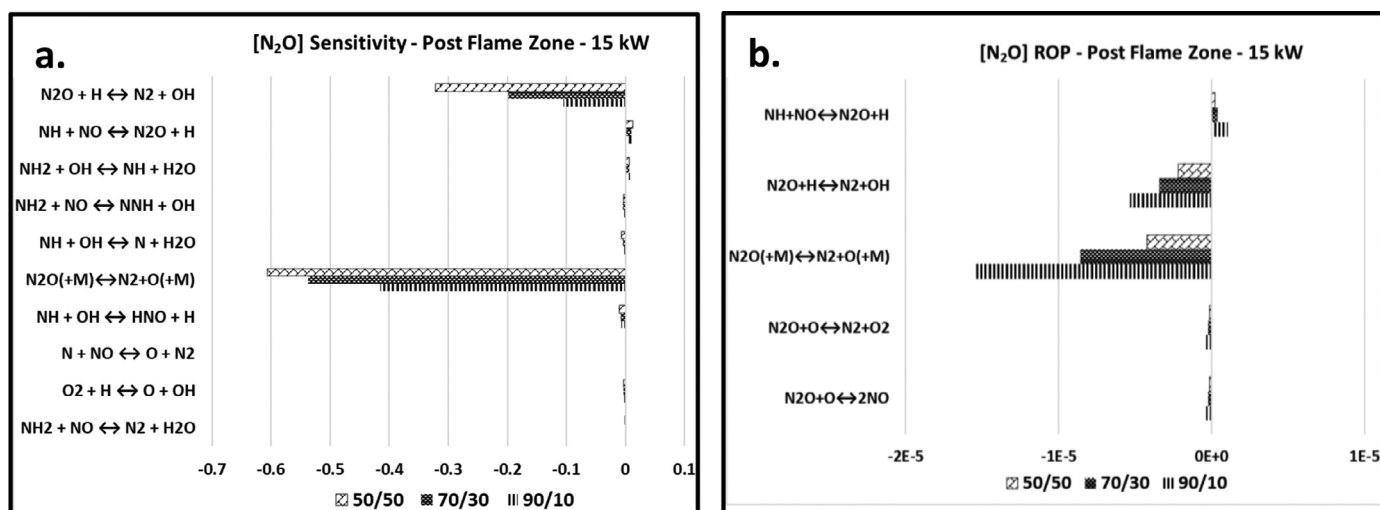


Fig. 17. Normalised sensitivity coefficients (a), and integrated ROP (b) of $[N_2O]$ at the post flame zone for 15 kW and fixed $\Phi = 0.65$. Unit of integrated ROP – mole/cm²-sec.

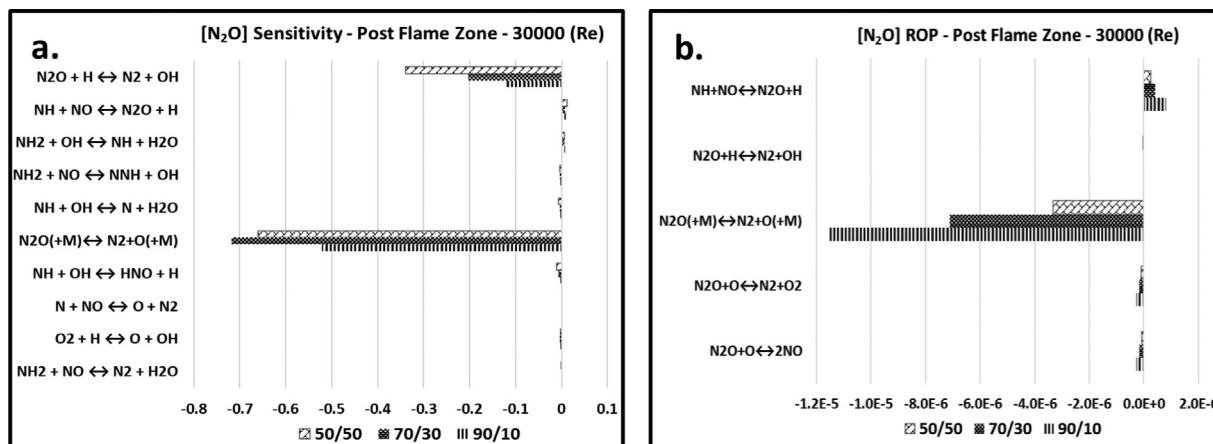


Fig. 18. Normalised sensitivity coefficients (a), and integrated ROP (b) of $[N_2O]$ at the post flame zone for $Re = 30,000$ and fixed $\Phi = 0.65$. Unit of integrated ROP – mole/cm²–sec.

the major route of N_2O reduction due to decrease in temperature, especially visible in Re conditions. These integrated ROP figures also validate previous observations regarding reduced N_2O productions at the PFZ. Fig. 19 shows the reaction rates of reaction R1, R2 and R3 against the distance at the post flame zone. Positive and negative reaction rates correspond to N_2O formation and reduction, respectively. Reaction rates for reaction R1 drops sharply to zero at the post flame zone, being R1 the only source of N_2O formation. N_2O formation decreases with increasing H_2 content in the flame. Reaction R3 remains active for longer at the post flame zone, compared to reaction R2, giving higher sensitivity and ROPs for R3 at the post flame zone, Figs. 17 and 18. As X_{NH_3} increases, hypothetically residence time increases due to lower flame reactivity and temperature decreases, resulting in higher reactivity for both reactions R2 and R3. Even then, measured N_2O showed the highest values with the 90/10_{VOL%} NH_3/H_2 blend due to increased N_2O formation at the flame zone. For comparison, at $Re = 30,000$ condition, N_2O drops from 1177 to 16 ppmv at the post flame zone for 50% NH_3 blend while for 90% NH_3 blend, N_2O reduces from 3883 to 198 ppmv.

4. Conclusions

Premixed NH_3/H_2 blends at different volumetric ratios with different thermal powers and Reynolds numbers at a fixed lean equivalence ratio (0.65) were investigated experimentally at a generic fuel-flexible swirl burner with a combination of spatially resolved OH^* , NH^* and NH_2^* chemiluminescence, spectrometry analysis and exhaust emissions measurements. The experimental conditions were evaluated numerically in Chemkin-Pro-environment to determine the reactions responsible for $[N_2O]$ and the changes in their reactivity as NH_3 concentrations in the fuel varied. Six recent ammonia mechanisms from the literature were employed in a model developed previously for swirling flames. The mechanism published by Stagni et al. [56] was chosen for the sensitivity analysis as its predictions by employing current CRN model were closest to the experimentally derived emissions results at the exhaust. The main conclusions of this investigation are summarised as follows.

1. NO and NO_2 emissions decreased with increasing ammonia content in the fuel due to the decreasing production of NH and OH radicals in the flames as these radicals combine together to produce HNO which is the main source of NO and NO_2 production. However, N_2O emissions followed opposite

- trend as NO is consumed with NH to produce N_2O . Increased N_2O emissions at high ammonia flames ($X_{NH_3} \geq 0.8$) were attributed to increased heat losses and greater production of NH radicals. NH_3 emissions at the exhaust were found to be minimum at $\Phi = 0.65$, except at 90/10_{VOL%} NH_3/H_2 blends as it went to LBO scenario due to reduced flame reactivity.
2. NH^* , OH^* and NH_2^* distribution in the flames increased with increasing ammonia content in the fuel as flame thickness increases. However, intensity of these radicals was found to be decreasing with decreasing H_2 mole fraction in the fuel blends. For thermal power conditions, radical intensities were observed to be increasing with thermal power but for above 80% NH_3 blends, 15 kW flames showed increased OH^* and NH^* intensities, resulting into most NO formations via HNO route. Similarly, considerably low NO productions at $Re = 20,000$ up to $X_{NH_3} = 0.7$ were also attributed to low radicals formations in the flames.
3. Detailed $[N_2O]$ sensitivity analysis displayed substantial N_2O formation at the flame zone through the reaction $NH + NO \leftrightarrow N_2O + H$. Reaction rate of this reaction increased with increasing ammonia contents in the fuel as flame temperature dropped. Significant amount of N_2O formed at the flame zone converted to N_2 at the post flame zone through the reactions $N_2O + H \leftrightarrow N_2 + OH$ and $N_2O(+M) \leftrightarrow N_2 + O(+M)$. Reaction rates for both these reactions increased with higher ammonia in the fuel due to higher residence time and lower temperature, whilst the latter reaction remained active for longer to reduce N_2O .
4. Overall, it was observed that lean ammonia/hydrogen combustion under industrially representative equivalence ratios may lead to the possibility of high N_2O emissions, limiting the applicability of the concept and potentially the direct, minor retrofitting of current gas turbines to employ ammonia/hydrogen blends operating under Dry Low NO_x technologies. However, further investigation is necessary at high pressure and at different swirl numbers to observe the effect on NO_x production and possible post-treatment technologies.

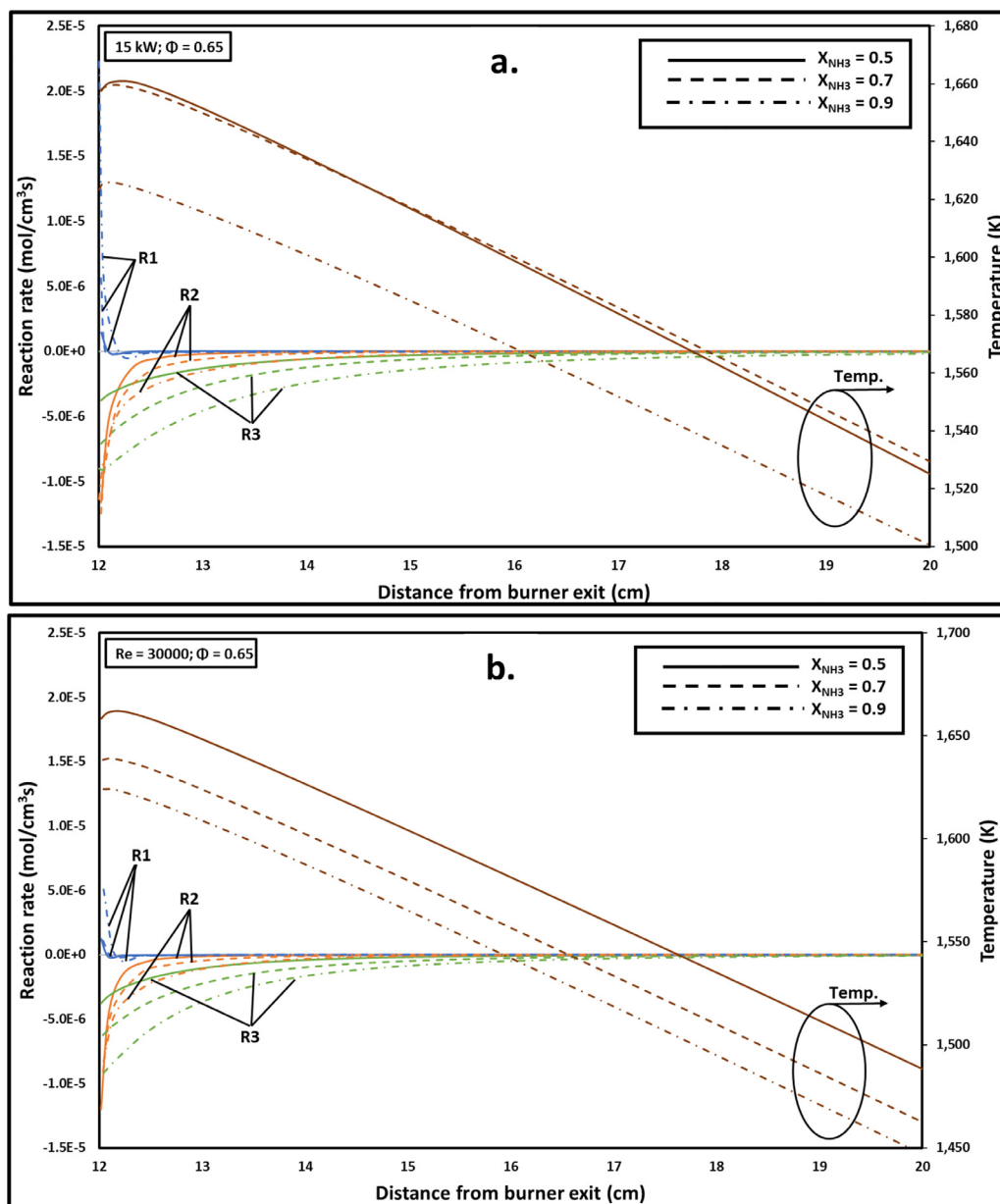


Fig. 19. Reaction rates for reactions R1, R2 and R3 and temperature distribution at the post flame zone for 15 kW (a) and $Re = 30,000$ (b). Positive and negative reaction rates correspond to N_2O production and consumption, respectively.

Declaration of Competing Interest

The authors declare that they have no known competing financial interests or personal relationships that could have appeared to influence the work reported in this paper.

Acknowledgements

This work was supported by the SAFE-AGT pilot (no. EP/T009314/1) with funding from the Engineering and Physical Sciences Research Council (EPSRC). The research was undertaken at Cardiff University's ThermoFluids Lab (W/0.17) with invaluable technical support from Mr. Malcolm Seaborne. Information on the data underpinning the results presented here, including how to access them, can be found in the Cardiff University data catalogue at <http://doi.org/10.17035/d.2022.0214909050>.

Supplementary materials

Supplementary material associated with this article can be found, in the online version, at doi:[10.1016/j.combustflame.2022.112299](https://doi.org/10.1016/j.combustflame.2022.112299).

References

- [1] O. Elishav, et al., Progress and prospective of nitrogen-based alternative fuels, *Chem. Rev.* 120 (12) (2020) 5352–5436, doi:[10.1021/acs.chemrev.9b00538](https://doi.org/10.1021/acs.chemrev.9b00538).
- [2] A. Valera-Medina, et al., Review on ammonia as a potential fuel: from synthesis to economics, *Energy & Fuels* 35 (9) (Feb. 2021) 6964–7029, doi:[10.1021/acs.energyfuels.0c03685](https://doi.org/10.1021/acs.energyfuels.0c03685).
- [3] A. Valera-Medina, A. Roldan, Ammonia from steelworks, *Green Energy Technol.* (2020) 69–80.
- [4] N. Salmon, R. Bañares-Alcántara, Green ammonia as a spatial energy vector: a review, *Sustain. Energy Fuels* (2021), doi:[10.1039/D1SE00345C](https://doi.org/10.1039/D1SE00345C).
- [5] A. Valera-Medina, D.G. Pugh, P. Marsh, G. Bulat, P. Bowen, Preliminary study on lean premixed combustion of ammonia-hydrogen for swirling gas turbine combustors, *Int. J. Hydrogen Energy* 42 (38) (2017) 24495–24503 [Online]. Available: <http://files/753/S0360319917332512.html>.

- [6] N.J. Duijm, F. Markert, and J.L. Paulsen, "Safety Assessment of Ammonia As a Transport Fuel," Denmark, 2005. [Online]. Available: <https://www.osti.gov/etdweb/servlets/purl/20607161>.
- [7] Quest Consultants Inc., "Comparative Quantitative Risk Analysis of Motor Gasoline, LPG and Anhydrous Ammonia As an Automotive Fuel," Iowa, USA, 2009. [Online]. Available: https://nh3fuel.files.wordpress.com/2013/01/nh3_riskanalysis_final.pdf.
- [8] S. Crollius, D.G. Pugh, S. Morris, and A. Valera-Medina, "Safety Aspects," in *Techno-economic challenges of ammonia as an energy vector*, Academic Press, 2020, p. 37.
- [9] O. Kurata et al., "Pure Ammonia Combustion Micro Gas Turbine System," 2019.
- [10] M. Guteša Božo, M.O. Viguera-Zuniga, M. Buffi, T. Seljak, A. Valera-Medina, Fuel rich ammonia-hydrogen injection for humidified gas turbines, *Appl. Energy* 251 (Oct. 2019) 113334, doi:10.1016/j.apenergy.2019.113334.
- [11] X. Jiang, R. Zhang, J. Chen, and Z. Huang, "Effect of hydrogen blending on the high temperature auto-ignition of ammonia at elevated pressure," 2021.
- [12] D. Thomas and W. Northrop, "Ammonia-Hydrogen Combustion in Diffusion Flames," 2021.
- [13] E.C. Okafor, et al., Experimental and numerical study of the laminar burning velocity of CH₄-NH₃-air premixed flames, *Combust. Flame* 187 (Jan. 2018) 185–198, doi:10.1016/j.combustflame.2017.09.002.
- [14] S.-E. Zitouni et al., "AMMONIA BLENDED FUELS-ENERGY SOLUTIONS FOR A GREEN FUTURE," 2021.
- [15] G.B. Ariemma, G. Sorrentino, R. Ragucci, M. de Joannon, P. Sabia, Ammonia/methane combustion: stability and NO_x emissions, *Combust. Flame* 241 (Jul. 2022) 112071, doi:10.1016/j.COMBUSTFLAME.2022.112071.
- [16] M. Zhang, et al., The regulation effect of methane and hydrogen on the emission characteristics of ammonia/air combustion in a model combustor, *Int. J. Hydrogen Energy* 46 (40) (2021) 21013–21025, doi:10.1016/j.ijhydene.2021.03.210.
- [17] D. Pugh, et al., Emissions performance of staged premixed and diffusion combustor concepts for an nh₃/air flame with and without reactant humidification, *J. Eng. Gas Turbines Power* (Dec. 2020) 1–10, doi:10.1115/1.4049451.
- [18] H. Xiao, A. Valera-Medina, P.J. Bowen, Modeling combustion of ammonia/hydrogen fuel blends under gas turbine conditions, *Energy & Fuels* 31 (8) (Aug. 2017) 8631–8642, doi:10.1021/acs.energyfuels.7b00709.
- [19] C. Netzer, A. Ahmed, A. Gruber, T. Løvås, Curvature effects on NO formation in wrinkled laminar ammonia/hydrogen/nitrogen-air premixed flames, *Combust. Flame* 232 (Oct. 2021) 111520, doi:10.1016/j.COMBUSTFLAME.2021.111520.
- [20] H. Kobayashi, A. Hayakawa, K.D.K.A. Somarathne, E.C. Okafor, Science and technology of ammonia combustion, *Proc. Combust. Inst.* (Nov. 2018), doi:10.1016/j.proci.2018.09.029.
- [21] Global Warming Potential Values, Jul. 30, 2021 Accessed:[Online]. Available: https://www.ghgprotocol.org/sites/default/files/ghgp/Global-Warming-Potential-Values%28Feb162016%29_1.pdf.
- [22] X. Zhu, A.A. Khatieb, T.F. Guiberti, W.L. Roberts, NO and OH* emission characteristics of very-lean to stoichiometric ammonia-hydrogen-air swirl flames, *Proc. Combust. Inst.* 38 (4) (2021) 5155–5162, doi:10.1016/j.proci.2020.06.275.
- [23] D. Stolten, B. Emonts, *Hydrogen Science and Engineering: Materials, Processes, Systems and Technology*, 1st ed., Wiley-VCH, 2016.
- [24] E.C. Okafor, et al., Control of NO_x and other emissions in micro gas turbine combustors fuelled with mixtures of methane and ammonia, *Combust. Flame* 211 (Jan. 2020) 406–416, doi:10.1016/j.combustflame.2019.10.012.
- [25] E.C. Okafor, et al., Influence of wall heat loss on the emission characteristics of premixed ammonia-air swirling flames interacting with the combustor wall, *Proc. Combust. Inst.* 38 (4) (Jan. 2021) 5139–5146, doi:10.1016/J.PROCI.2020.06.142.
- [26] A.A. Khatieb, T.F. Guiberti, X. Zhu, M. Younes, A. Jamal, W.L. Roberts, Stability limits and NO emissions of technically-premixed ammonia-hydrogen-nitrogen-air swirl flames, *Int. J. Hydrogen Energy* 45 (41) (Aug. 2020) 22008–22018, doi:10.1016/j.ijhydene.2020.05.236.
- [27] K.P. Shrestha, et al., An experimental and modeling study of ammonia with enriched oxygen content and ammonia/hydrogen laminar flame speed at elevated pressure and temperature, *Proc. Combust. Inst.* 38 (2) (Jan. 2021) 2163–2174, doi:10.1016/j.proci.2020.06.197.
- [28] X. He, B. Shu, D. Nascimento, K. Moshhammer, M. Costa, R.X. Fernandes, Auto-ignition kinetics of ammonia and ammonia/hydrogen mixtures at intermediate temperatures and high pressures, *Combust. Flame* (2019), doi:10.1016/j.combustflame.2019.04.050.
- [29] H. Xiao, A. Valera-Medina, Chemical kinetic mechanism study on premixed combustion of ammonia/hydrogen fuels for gas turbine use, *J. Eng. Gas Turbines Power* 139 (8) (Apr. 2017), doi:10.1115/1.4035911.
- [30] B. Mei, et al., Experimental and kinetic modeling investigation on the laminar flame propagation of ammonia under oxygen enrichment and elevated pressure conditions, *Combust. Flame* 210 (2019) 236–246, doi:10.1016/j.combustflame.2019.08.033.
- [31] UC San Diego, "Chemical kinetic mechanisms," Combustion Research Group, 2021.
- [32] A. Gaydon, *The spectroscopy of flames*. 2012.
- [33] K. Ohashi, T. Kasai, D.C. Che, K. Kuwata, Alignment dependence of the amidegen chemiluminescence in the reaction of argon(3P) atoms with the aligned ammonia molecules, *J. Phys. Chem.* 93 (14) (2002) 5484–5487, doi:10.1021/J100351A033.
- [34] G.L. Schott, L.S. Blair, D.M. J. Jr., Exploratory shock-wave study of thermal nitrogen trifluoride decomposition and reactions of nitrogen trifluoride and dinitrogen tetrafluoride with hydrogen, *J. Phys. Chem.* 77 (24) (2002) 2823–2830, doi:10.1021/J100642A001.
- [35] T.R. Roose, R.K. Hanson, C.H. Kruger, A shock tube study of the decomposition of no in the presence of NH₃, *Symp. Combust.* 18 (1) (Jan. 1981) 853–862, doi:10.1016/S0082-0784(81)80089-6.
- [36] Y. Yi, R. Zhang, L. Wang, J. Yan, J. Zhang, H. Guo, Plasma-triggered CH₄/NH₃ coupling reaction for direct synthesis of liquid nitrogen-containing organic chemicals, *ACS Omega* (2017), doi:10.1021/acsomega.7b01060.
- [37] S. Mashruk, "NO Formation Analysis using Chemical Reactor Modelling and LIF Measurements on Industrial Swirl Flames - PhD Thesis," Cardiff University, 2020.
- [38] M.J. Bedard, T.L. Fuller, S. Sardeshmukh, W.E. Anderson, Chemiluminescence as a diagnostic in studying combustion instability in a practical combustor, *Combust. Flame* 213 (Mar. 2020) 211–225, doi:10.1016/J.COMBUSTFLAME.2019.11.039.
- [39] S. Mashruk, et al., Combustion features of CH₄/NH₃/H₂ ternary blends, *Int. J. Hydrogen Energy* (Apr. 2022), doi:10.1016/j.ijhydene.2022.03.254.
- [40] D. Pugh, et al., An investigation of ammonia primary flame combustor concepts for emissions reduction with OH*, NH₂* and NH* chemiluminescence at elevated conditions, *Proc. Combust. Inst.* 38 (4) (Sep. 2021) 6451–6459, doi:10.1016/j.proci.2020.06.310.
- [41] C.R. Shaddix, A new method to compute the proper radiating heat transfer correction of bare-wire thermocouple measurements, Proceedings of the 10th U.S. National Combustion Meeting, 2017–April (2017) Accessed: May 04, 2022. [Online]. Available: .
- [42] British Standard, BS ISO 11042-1:1996. Gas Turbines-Exhaust Gas Emission, 1996.
- [43] S. Mashruk, H. Xiao, A. Valera-Medina, Rich-Quench-Lean model comparison for the clean use of humidified ammonia/hydrogen combustion systems, *Int. J. Hydrogen Energy* 46 (5) (Jan. 2020) 4472–4484, doi:10.1016/j.ijhydene.2020.10.204.
- [44] M. Guteša Božo, S. Mashruk, S. Zitouni, A. Valera-Medina, Humidified ammonia/hydrogen RQL combustion in a trigeneration gas turbine cycle, *Energy Convers. Manag.* 227 (Jan. 2021) 113625, doi:10.1016/j.enconman.2020.113625.
- [45] S. Mashruk, et al., Numerical analysis on the evolution of NH₂ in ammonia/hydrogen swirling flames and detailed sensitivity analysis under elevated conditions, *Combust. Sci. Technol.* 00 (00) (2021) 1–28, doi:10.1080/00102202.2021.1990897.
- [46] M. Viguera-Zuniga, M. Tejada-del-Cueto, J. Vasquez-Santacruz, A. Herrera-May, A. Valera-Medina, Numerical predictions of a swirl combustor using complex chemistry fueled with ammonia/hydrogen blends, *Energies* 13 (2) (2020) 288, doi:10.3390/en13020288.
- [47] A. Valera-Medina, N. Syred, P. Bowen, Central recirculation zone visualization in confined swirl combustors for terrestrial energy, *J. Propuls. Power* 29 (1) (2013), doi:10.2514/1.B34600.
- [48] R. d'Agostino, F. Cramarossa, S. De Benedictis, G. Ferraro, Kinetic and spectroscopic analysis of NH₃ decomposition under R.F. Plasma at moderate pressures, *Plasma Chem. Plasma Process.* 1 (1) (1981) 19–35, doi:10.1007/BF00566373.
- [49] J. Ballester, T. García-Armingol, Diagnostic techniques for the monitoring and control of practical flames, *Prog. Energy Combust. Sci.* 36 (4) (Aug. 2010) 375–411, doi:10.1016/j.pecs.2009.11.005.
- [50] S.L. Sheehe, S.I. Jackson, Spatial distribution of spectrally emitting species in a nitromethane-air diffusion flame and comparison with kinetic models, *Combust. Flame* 213 (Mar. 2020) 184–193, doi:10.1016/J.COMBUSTFLAME.2019.10.026.
- [51] J.H. Lee, S.I. Lee, O.C. Kwon, Effects of ammonia substitution on hydrogen/air flame propagation and emissions, *Int. J. Hydrogen Energy* 35 (20) (2010) 11332–11341, doi:10.1016/j.ijhydene.2010.07.104.
- [52] M.O. Viguera-Zuniga, M.E. Tejada-Del-cueto, S. Mashruk, M. Kovaleva, C.L. Ordóñez-Romero, A. Valera-Medina, Methane/ammonia radical formation during high temperature reactions in swirl burners, *Energies* 14 (20) (2021) 6624, doi:10.3390/EN14206624.
- [53] D. Pugh, P. Bowen, A. Valera-Medina, A. Giles, J. Runyon, R. Marsh, Influence of steam addition and elevated ambient conditions on NO_x reduction in a staged premixed swirling NH₃/H₂ flame, *Proc. Combust. Inst.* 37 (4) (2019) 5401–5409, doi:10.1016/j.proci.2018.07.091.
- [54] X. Zhang, S.P. Moosakutty, R.P. Rajan, M. Younes, S.M. Sarathy, Combustion chemistry of ammonia/hydrogen mixtures: jet-stirred reactor measurements and comprehensive kinetic modeling, *Combust. Flame* 234 (2021) 111653, doi:10.1016/J.COMBUSTFLAME.2021.111653.

- [55] G.J. Gotama, et al., Measurement of the laminar burning velocity and kinetics study of the importance of the hydrogen recovery mechanism of ammonia/hydrogen/air premixed flames, *Combust. Flame* (2021).
- [56] Alessandro Stagni, et al., An experimental, theoretical and kinetic-modeling study of the gas-phase oxidation of ammonia, *React. Chem. Eng.* 5 (4) (2020) 696–711, doi:[10.1039/C9RE00429G](https://doi.org/10.1039/C9RE00429G).
- [57] H. Nakamura, M. Shindo, Effects of radiation heat loss on laminar premixed ammonia/air flames, *Proc. Combust. Inst.* 37 (2) (2019) 1741–1748, doi:[10.1016/J.PROCI.2018.06.138](https://doi.org/10.1016/J.PROCI.2018.06.138).
- [58] M.V. Manna, P. Sabia, G. Sorrentino, T. Viola, R. Ragucci, M. de Joannon, New insight into NH₃-H₂ mutual inhibiting effects and dynamic regimes at low-intermediate temperatures, *Combust. Flame* (2022) 111957, doi:[10.1016/J.COMBUSTFLAME.2021.111957](https://doi.org/10.1016/J.COMBUSTFLAME.2021.111957).
- [59] A.C. Benim, K.J. Syed, Flashback mechanisms in lean premixed gas turbine combustion, *Flashback Mech. Lean Premixed Gas Turbine Combust.* (2014) 1–123, doi:[10.1016/C2013-0-18847-2](https://doi.org/10.1016/C2013-0-18847-2).
- [60] W. Rodi, Engineering turbulence modelling and experiments 6, *Eng. Turbul. Model. Exp.* 6 (2005), doi:[10.1016/B978-0-08-044544-1.X5000-6](https://doi.org/10.1016/B978-0-08-044544-1.X5000-6).
- [61] P. Glarborg, J.A. Miller, B. Ruscic, S.J. Klippenstein, Modeling nitrogen chemistry in combustion, *Prog. Energy Combust. Sci.* 67 (2018) 31–68, doi:[10.1016/j.peecs.2018.01.002](https://doi.org/10.1016/j.peecs.2018.01.002).
- [62] J. Otomo, M. Koshi, T. Mitsumori, H. Iwasaki, K. Yamada, Chemical kinetic modeling of ammonia oxidation with improved reaction mechanism for ammonia/air and ammonia/hydrogen/air combustion, *Int. J. Hydrogen Energy* (2018), doi:[10.1016/j.ijhydene.2017.12.066](https://doi.org/10.1016/j.ijhydene.2017.12.066).
- [63] Z. Tian, Y. Li, L. Zhang, P. Glarborg, F. Qi, An experimental and kinetic modeling study of premixed NH₃/CH₄/O₂/Ar flames at low pressure, *Combust. Flame* 156 (7) (2009) 1413–1426, doi:[10.1016/j.combustflame.2009.03.005](https://doi.org/10.1016/j.combustflame.2009.03.005).